

pubs.acs.org/JPCL Letter

Development and Validation of Versatile Deep Atomistic Potentials for Metal Oxides

Pandu Wisesa, Christopher M. Andolina, and Wissam A. Saidi*



Cite This: J. Phys. Chem. Lett. 2023, 14, 468-475



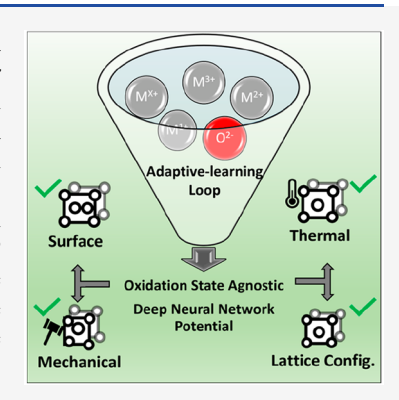
ACCESS I

Metrics & More

Article Recommendations

Supporting Information

ABSTRACT: Machine learning interatomic potentials powered by neural networks have been shown to readily model a gradient of compositions in metallic systems. However, their application to date on ionic systems tends to focus on specific compositions and oxidation states owing to their more heterogeneous chemical nature. Herein we show that a deep neural network potential (DNP) can model various properties of metal oxides with different oxidation states without additional charge information. We created and validated DNPs for Ag_xO_y, Cu_xO_y Mg_xO_y, Pt_xO_y and Zn_xO_y, whereby each system was trained without any limitations on oxidation states. We illustrate how the database can be augmented to enhance the DNP transferability for a new polymorph, surface energies, and thermal expansion. In addition, we show that these potentials can correctly interpolate significant pressure and temperature ranges, exhibit stability over long molecular dynamics simulation time scales, and replicate nonharmonic thermal expansion, consistent with experimental results.



omputational modeling of materials provides a unique insight into materials phenomenon at a granular level, which can be leveraged to explain trends seen in experiments or help guide experimental approaches. Density functional theory (DFT) is the tool of choice to model materials at an atomistic level due to its accuracy over traditional molecular dynamics (MD) approaches driven by interatomic potentials. However, for large system sizes and/or longer time scales, i.e., scales that approach experimental observation, DFT methodologies are challenging due to the significant increase in computational cost and system scaling. Bridging this gap is where interatomic potentials prevail due to their capability to compute atomic interactions much more rapidly.

The development of interatomic potentials for various materials is an ongoing continuous effort that has spanned over six decades. Each interatomic potential model typically focuses on a specific type of atomic interaction and generally follows the bond order. Developing models for ionic solids, such as metal oxides, is nontrivial as the electronic polarization, and charges in the material must be described. While many-body potentials such as reactive force field (ReaxFF)² and charge optimized many-body (COMB)³ potentials have shown some success in describing ionic systems, these potentials do not exist for a wide variety of systems, partly because of the considerable effort needed to construct them. Therefore, there is a need to rapidly develop interatomic potentials for ionically bonded materials to model large systems efficiently.

The application of machine learning has fueled the recent creation of transferrable and efficient machine learning interatomic potentials.^{4–8} In contrast to conventional force fields, these potentials differ in that they do not use parametric functional forms, but instead, the interatomic interactions are

inferred from a given data set. There have been several variants of these potentials. For instance, the Gaussian approximation potential⁴ uses Gaussian process regression to model the potential energy surface. Similarly, the moment tensor potential⁵ combines invariant polynomials and linear regression. Both methods have been shown to model various material aspects successfully. An alternative to using regression-based processes is leveraging neural networks as a statistical processor, whereby the weight for any given input is inherently interconnected to all others, akin to how the brain works; these potentials are known as neural network potentials.

There are various approaches to using neural networks to represent potential energy surfaces. 10,11 Behler and Parrinello 12 proposed a generalized form that uses a neural network to fit a given functional form with atomic coordinates as inputs to describe the system more generally. Similarly, Schütt et al. 13 created a deep tensor neural network that utilized a vector of nuclear charges and an interatomic distance matrix as inputs. Han et al. 14 used multilayered neural networks where each atom is represented by a small subnetwork, which scales with the number of atom neighbors with a prescribed cutoff radius; potentials generated with schemes involving multiple neural network layers are more commonly known as deep neural network potentials (DNPs). Previous studies have shown that

Received: November 12, 2022 Accepted: January 5, 2023 Published: January 9, 2023





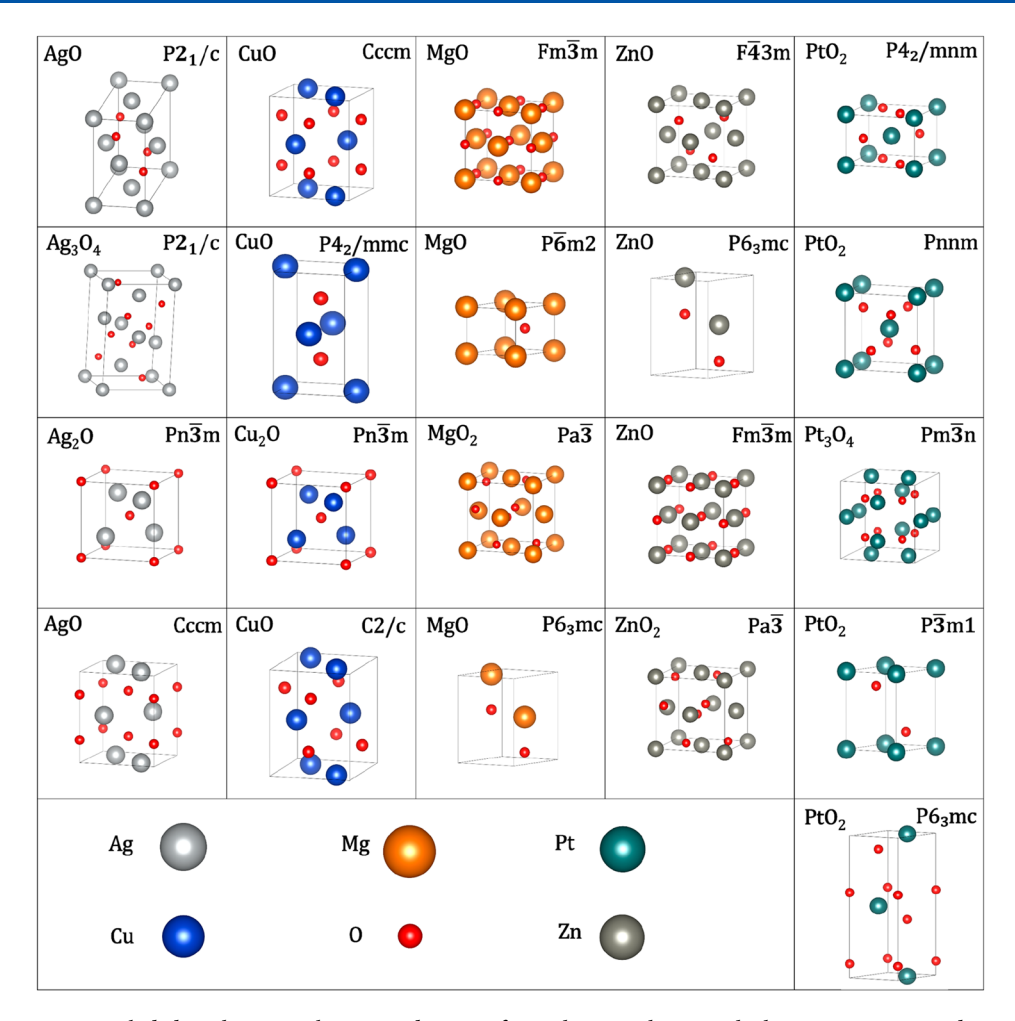


Figure 1. Parent structures included in the original training data sets for each DNP shown with their composition and space group. Structure images were generated using VESTA.³⁶

DNPs replicate DFT values reliably. ^{15–26} For instance, DNPs have been applied to elemental metals ^{16–18} and binary metal alloys, e.g., Cu–Zr, ¹⁶ Au–Ag, ¹⁷ and Al–Mg, ¹⁸ as well as higher metal alloy systems such as Al–Cu–Ni¹⁹ and even for high entropy alloys. ²⁰ Also, DNPs have been successfully applied to several systems with covalent bonding, such as water ^{22–25} and Ga. ²⁶

In contrast, fewer studies have been performed on ionic materials, such as the investigation of polymorphism in HfO_2 , viscosity and electrical conductivity of $MgSiO_4$, metal halide perovskites, and thermal conductivity of β - Ga_2O_3 . In these studies, the application of DNPs was focused on a limited set of oxidation states. This is, in part, an acknowledgment of the complexities that comes with the nature of ionic bonding. Traditional force fields generally have limited transferability when applied to ionic systems with different oxidation states. Thus, it is unclear how DNPs fare when applied to ionic systems in general and their capabilities in describing multiple oxidation states for a given metal.

To address this research gap, we conduct a systematic investigation by developing five metal oxygen DNPs: Ag_xO_y , Cu_xO_y , Mg_xO_y , Pt_xO_y , and Zn_xO_y . We used an adaptive-learning process to establish the DNPs and validate the results with DFT values. We quantitatively demonstrate that DNPs can describe metal oxide surfaces with near-DFT accuracy. In addition, we demonstrate for MgO how the data sets originally

constructed to describe periodic systems at low temperatures can be appropriately augmented to enhance the transferability of the DNPs toward other properties of the systems such as thermal expansion which requires long MD simulations at temperatures near the melting point.

The DFT calculations to generate the data sets for DNP training were done with Vienna *Ab initio* Simulation Package (VASP).^{31–33} The DNPs were developed with the DeepPot-SE method²⁰ as implemented in DeePMD-Kit.⁶ The atomistic calculations using the DNP were performed using LAMMPS.³⁴ See the Supporting Information for further details and convergence checking.

The initial training structures were taken from the Materials Project database (MPDB).³⁵ While it is possible to include all the available oxide structures in MPDB for each oxide, we opted to limit the number of initial training structures to four or five per metal, focusing on the experimentally verified and stable structures; i.e., structures whose energy above the hull is higher than 0.4 eV/atom are not included. The motivation behind the selection is to develop DNPs of broader interest for further studies.

In addition to selecting distinct symmetries to test the capability of DNPs in describing a variety of ionic systems, at least two different metal oxidation states are included for each system. Namely, for Ag_xO_y , we include cubic Ag_2O , monoclinic Ag_3O_4 , and monoclinic as well as orthorhombic AgO. For

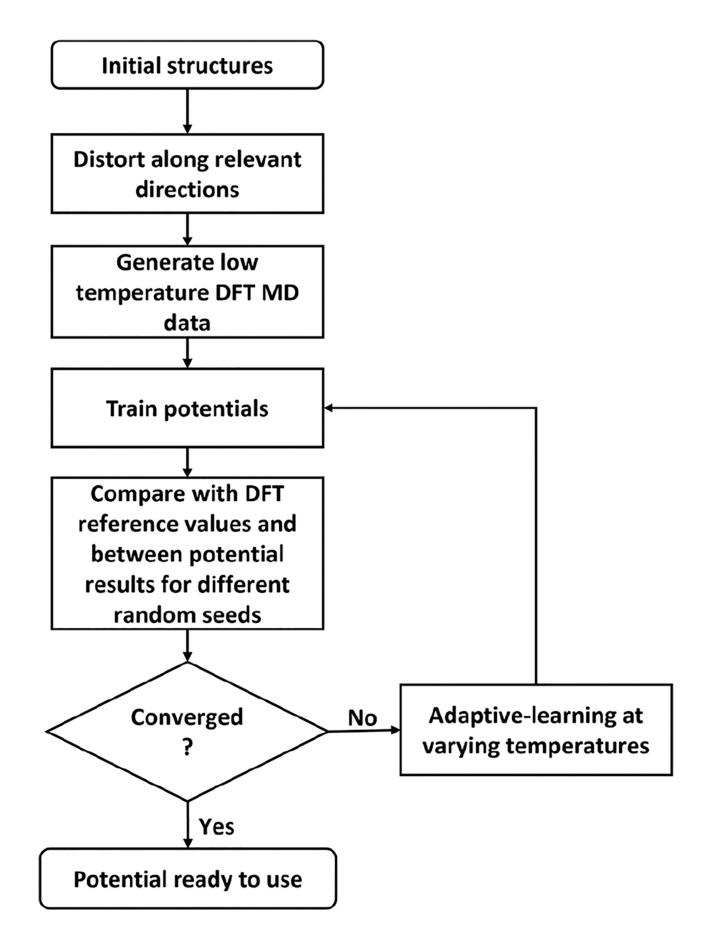
 $\text{Cu}_x \text{O}_y$, we choose the cubic $\text{Cu}_2 \text{O}$, monoclinic, tetragonal, and orthorhombic CuO. For $\text{Mg}_x \text{O}_y$, we include cubic MgO_2 , rock salt MgO, and $P6_3mc$ as well as $P\overline{6}m2$ hexagonal MgO. For $\text{Pt}_x \text{O}_y$, we include tetragonal, orthorhombic, trigonal, and hexagonal PtO_2 along with cubic $\text{Pt}_3 \text{O}_4$. Finally, for $\text{Zn}_x \text{O}_y$, we select cubic ZnO_2 , rock salt ZnO, cubic $F\overline{4}3m$, and hexagonal ZnO. The selected structures are shown in Figure 1 and will be termed parent structures from now on. More details on these parent structures can be found in the Supporting Information.

We want to emphasize that one of our goals in this study is to create "starter" DNPs and versatile data sets that can facilitate future studies. Thus, other researchers will utilize all or part of the existing training data, e.g., based on temperature or symmetry, to develop DNPs apt for describing properties of their choice.

A lack of systematic study in training metal oxides makes replicating existing studies from scratch challenging. Considering the number of metal oxides involved in this study, it would be beneficial to establish reference points to training the potential and augmenting it when necessary. This would provide guidelines and information for others to train similar systems or how to tailor the existing DNPs for future studies.

We employed the following protocol to generate the training data set, as shown in Scheme 1. Starting from the optimized parent structure of a given system, additional structures with lattice distortions δ of the magnitude of $\pm 1\%$ in multiple combinations from directions X, Y, Z, XY, XZ, and YZ for both the unit cell and $2 \times 2 \times 2$ supercell were generated. To account for different atomic environments, it is recommended

Scheme 1. DNP Training Process Utilized in This Study



to choose relatively large values for δ . However, we found that distortion magnitudes larger than ±1% could lead to atoms being unphysically separated, especially for larger unit cells. Using the distorted initial structures, we conducted ab initio molecular dynamics simulations with NVT ensemble (constant-volume and temperature ensemble) for 20 steps at two temperatures: 250 and 500 K. We chose relatively low temperatures in consideration of the elastic constant calculations that are run at 0 K. In the first iteration of the potential, we utilized ~1800 configurations per parent structure. We then applied an iterative adaptive-learning process using an ensemble approach to improve the fidelity of the potential.³⁷ The process was performed by running MD NVT simulations using 3 versions of the potential obtained with different random seeds. In this process, we run DNP NVT simulations for 10 at 0.002 ps per step with 0.01 ps temperature damping at the two temperatures employed to generate the data set. The configurations with model deviations of the atomic forces between 0.2 and 1.0 eV/Å were selected and computed with DFT.³⁷ We run DFT NVT with ten ionic steps at 2 fs per step for each labeled structure to augment the database and develop a new version of the DNP. When this process converged and was deemed necessary, as explained in the following paragraph, we increased the temperature of the adaptive-learning loop to 750 and 1000 K and repeated the adaptive-learning process. These two high temperatures were chosen to create unique atomic environments. This process is considered converged once no model deviations are found above ~0.2 eV/Å. This cutoff was chosen empirically based on validation steps, as we show below.

In addition to model deviations, we found that regular examinations of physical properties, such as cohesive energies, lattice vectors, and elastic constants, can provide additional information in guiding the training by acting as another indicator for configurations that need to be included. Incorporating the comparison of physical properties in the determination of convergence can also expedite the training, especially if there is a specific target property, as we found them to tend to converge before the deviation go below $0.2 \, {\rm eV/\mathring{A}}$.

The employed adaptive-learning process converged after six for Ag_xO_y , four for Cu_xO_y and Pt_xO_y , and two iterations for Mg_xO_y and Zn_xO_y . The final data sets have, on average, ~3388 configurations per parent structure, with the total number for each system listed in Table S2.

The simplest way to quantify the performance of the DNPs is to compare the material properties at thermodynamic equilibrium. In the comparison shown in Figure 2a,b, cohesive energy and equilibrium volume are used as such metrics. The reported error bars in these figures represent the deviation over different parent structures. The DNP values are averaged over three different potentials. The root-mean-square-error (RMSE) values between DFT and DNP of the cohesive energy and volume comparisons are 0.026 eV and 0.050 Å $^3/$ atom, respectively.

The most significant difference between DFT and DNP in volume is for Ag_3O_4 , space group is $P2_1/c$, with a difference of 1.2 ų or 0.61%. The largest cohesive energy difference is 0.023 eV or 0.39% for PtO₂, space group $P6_3mc$. As seen in the figures, DNP results compare well to DFT, which indicates the versatility of the neural-network potentials, in which, once they have been trained sufficiently, the potentials can well describe oxides with different symmetries and oxidation states. For

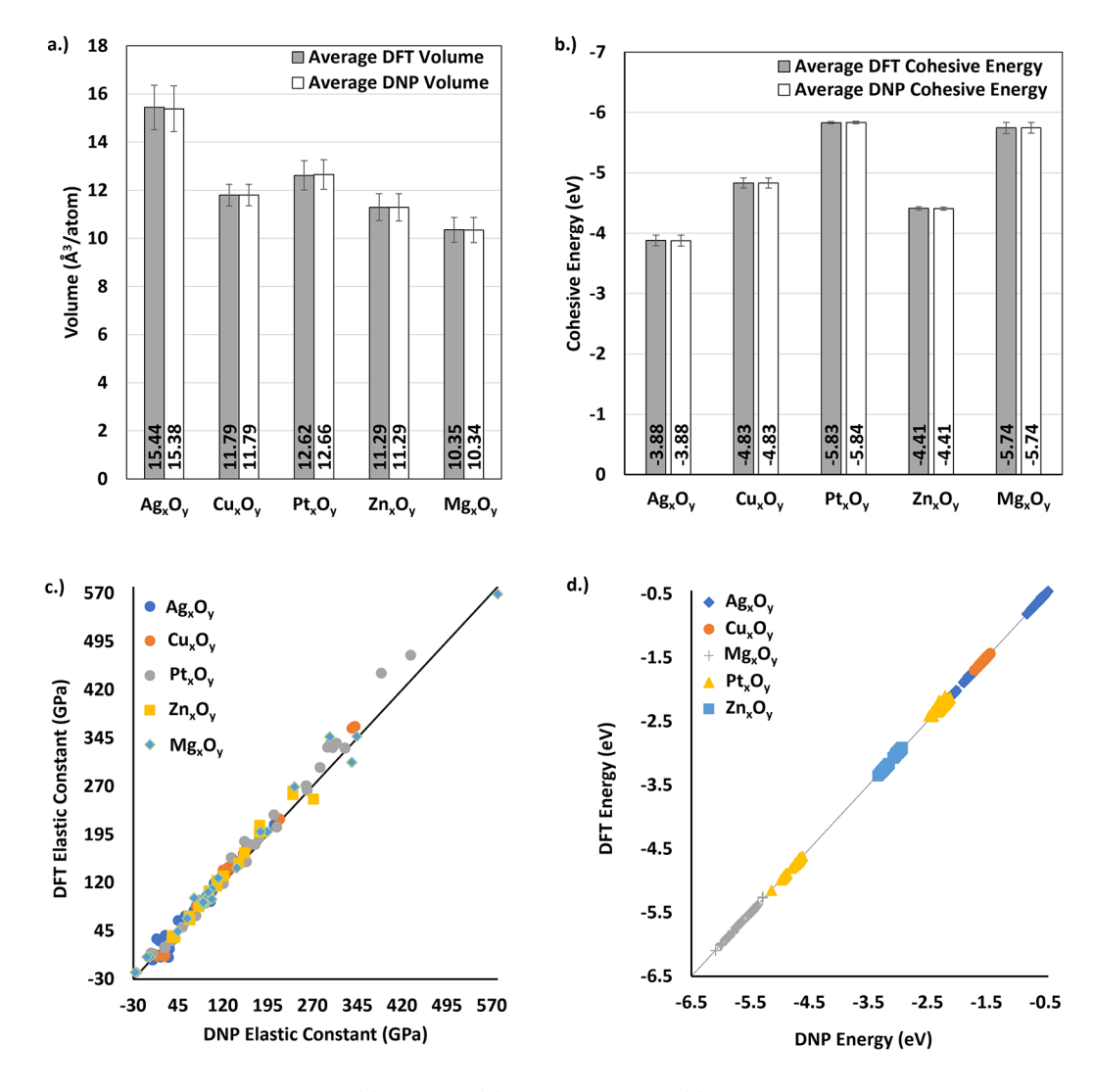


Figure 2. Comparison of DNP values vs DFT for (a) volumes, (b) cohesive energies, (c) elastic constants for all structures C11, C22, C33, C12, C13, C23, C44, C55, and C66, and (d) cohesive energy parity plot for structures randomly generated. (a, b) DNP values are averages over the different parent structures. All DNP values listed are normalized combinations over the ensembles of three different potentials. The RMSEs are (a) $0.050 \text{ Å}^3/\text{atom}$, (b) 0.026 eV, (c) 14 GPa, and (d) 0.021 eV.

instance, in the Ag_xO_y system, the physical properties of AgO and Ag_3O_4 that have distinct oxidation states even though they have the exact symmetry, $P2_1/c$, are described well by the potential. Similarly, the potential successfully describes the two AgO structures with the same oxidation states yet different lattices, monoclinic and orthorhombic. These trends are observed across the different oxide systems.

In addition to equilibrium properties, we also examined the elastic constants; this property measures the strength and nature of atomic bonds in the elastic limit. Computationally acquiring these values requires the DNPs to simulate materials at states beyond equilibrium, which is a good test of how the DNP copes when lattice symmetries are broken, a modeling challenge different from cohesive energy and volume calculations. Because elastic constants are not explicitly included in the data set, their validation also functions as an evaluation of the ability of the potential to extrapolate. A finite central difference method was employed to obtain the values from both DFT³⁸ and DNP. This process involved distorting the lattice in 12 directions followed by atomic relaxation. The stress—strain relationship is then used on the information

gained to calculate the elastic constants. With the variation of symmetries and composition, the elastic constant values shown in Figure 2c range from –25 to 579 GPa, with the RMSE being 14 GPa. The most significant difference in the elastic constant between the DFT and DNP values is 60 GPa (13.4%) for PtO₂ with *Pnnm* symmetry. Also, see Figure S3 comparing forces between DFT and DNP for all structures associated with elastic constant calculations.

We also assessed the transferability of the DNPs to configurations that are not included in the training set. We generated 200 random configurations using the DNP approach discussed earlier to create training data. This is applied to all parent structures. Figure 2d compares the energies for these structures to those obtained from DFT; the overall RMSE of this comparison is 0.021 eV. As seen in Figure 2, these potentials yield similar energy values as DFT, even for randomly generated configurations. A detailed breakdown of the cohesive energies, volumes, and elastic constants can be found in the Supporting Information.

The DNPs have shown good performances for bulk configurations based on the structures in the data set. The

Table 1. Energy and Volume of the Mg_xO_y Structures as Calculated by DFT and DNP before and after Training^a

structure		DFT		DNP before retraining		DNP after retraining	
composition	space group	cohesive energy (eV)	volume (ų/atom)	cohesive energy (eV)	volume (ų/atom)	cohesive energy (eV)	volume (ų/atom)
MgO_2	$P\overline{1}$	-5.64	11.40	-8.37	64.05	-5.61 (32.93%)	11.41 (82.19%)
MgO	$Fm\overline{3}m$	-5.94	76.60	-5.92	76.71	-5.93 (0.02%)	76.68 (0.04%)
MgO	$P\overline{6}m2$	-5.26	19.94	-5.29	19.89	-5.29 (0.02%)	19.92 (0.18%)
MgO_2	$Pa\overline{3}$	-9.06	116.84	-9.05	116.80	-9.07 (0.12%)	116.93 (0.11%)
MgO	$P6_3mc$	-5.79	48.54	-5.80	48.36	-5.80 (0.03%)	48.36 (0.01%)
a							

^aThe added structure is listed first. Values inside the parentheses indicate the percent change before and after retraining.

next question is how to expand a DNP to new structures or properties that were not explicitly included in the training database. While it is feasible to start from scratch, as shown in Scheme 1 and employed before, here, we augment the existing data set with relevant configurations to extend the transferability of the DNP.

In this demonstration, the Mg_xO_y data set was chosen as it is the smallest, as seen in Table S2. All Mg_xO_y structures (24 in total) from MPDB not included in the training were evaluated with DFT to get reference energy values and DNP to gauge its performance. Of the 24 assessed structures, the DNP predicted that the cohesive energy difference for 18 structures is <0.05 eV compared to the DFT reference values. Among the six structures expected to be the worst, the triclinic MgO₂ with 12 atoms, MPDB ID of mp-1245393, was chosen for this demonstration as the Mg_xO_y DNP performed the poorest for this structure. We followed the same training protocol as discussed before with the triclinic MgO2 by using initial structures with lattice distortions for the primitive unit cell and $2 \times 2 \times 2$ supercell as inputs for the adaptive-learning phase. Table 1 shows the calculated energy and volume of the newly added triclinic MgO₂ and the other MgO structures initially included in the DNP after one additional training iteration. It is important to see that the newly added structure creates no significant changes to the results of the old structures initially included in the database. However, in contrast, for triclinic MgO₂, there is a substantial improvement in the performance of the DNP. As seen in Table 1, the difference between energy calculated by the potential and DFT improved from 0.92 to 0.01 eV. In addition, the volume difference went down to within 0.1% of DFT.

The training process added 1578 new configurations, with 638 configurations $2 \times 2 \times 2$ supercells and the remaining 940 configurations being unit cells of triclinic MgO₂; most configurations are unit cells consisting of 12 atoms. The generation of the additional training data compared to the average starting data set is lower by 14.9% and by 52.7% compared to the average number of configurations per structure for DNP that reached parity, thereby illustrating that the adaptive-learning process can readily integrate new structures. Additionally, there are likely resource savings to consider when the adaptive-learning loop is leveraged to augment the accuracy of the original potential training data set.

We then extended the DNP to aperiodic systems focusing on the surface properties of MgO rock salt, which has been well studied before, e.g., chemical reactions.³⁹ Due to its cubic symmetry, the MgO rock salt has three possible surface orientations: (100), (110), and (111). On the basis of their ionic orientation, it can be expected for the (100) surface to be the most stable, followed by the (110) surface, with the (111) surface requiring some level of defects or reconstruction to be stable.⁴⁰ Herein, we focus on the stable (100) and (110)

surfaces as studying different reconstruction possibilities of (111) surfaces would be beyond the scope of this study.

Using the adaptive-learning loop, we trained the MgxOy potential with configurations from (100) and (110) surfaces. This process added 2076 surface configurations to the original data set. We used slab models with thicknesses of 10 and 20 Å. This corresponds to 6 and 12 layers for the (100) surface and for the (110) surface 8 and 14 layers. The vacuum gap was set to be 10 Å, and it is considered to be sufficient based on the study by Evarestov and Bandura⁴¹ which showed convergence of MgO (100) surface for a vacuum gap of at least 6.315 Å.

Consistent with the prediction from the ionic orientation, both DFT and DNP find the (100) surface to be more stable than the (110) surface. On the slab thickness, 10 and 20 Šreturn a surface energy difference of <2% for the (100) surface and <5% for the (110) surface. These differences are less than the error compared to the DFT results, which are 5.9% for the (100) surface and 7.8% for the (110) surface, with the standard deviation from the ensemble approach being 1.8 meV/Ų, as shown in Figure 3. Evarestov and Bandura 41 reported that the

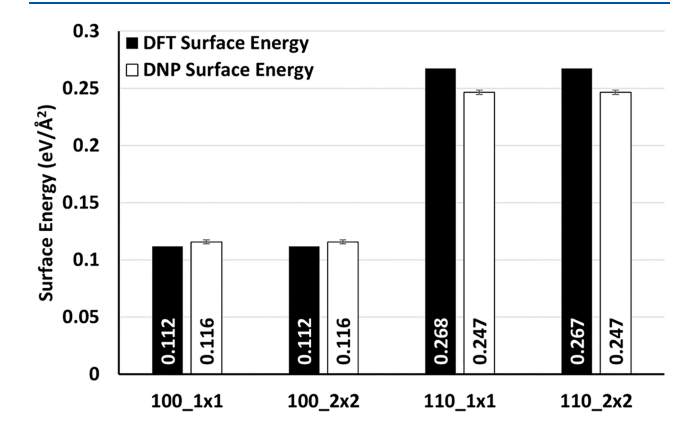


Figure 3. Comparison of DFT surface energy of MgO in black bars and the average DNP surface energies from ensemble approach in white bars.

MgO (100) surface energy starts to converge at 5 layers of MgO with surface energy values of 0.0958 eV/Ų for 6 and 12 layers of MgO; this is a difference of 0.016 eV/Ų compared to our DFT result and 0.020 eV/Ų compared to the DNP.

Compared to the experimental value by Jura and Garland⁴² of 0.0649 eV/Å² for the MgO surface energy, both DFT and DNP calculations overestimate the surface energy by 41.9%. Lazar and Otyepka⁴³ argued that the overestimation of PBE surface energy calculation could be mitigated using exact exchange and random phase approximation methodology. For this study, we limit our DFT calculations to PBE functional.

Simulating thermal expansion is an excellent test of the transferability of the potential. The process involves running

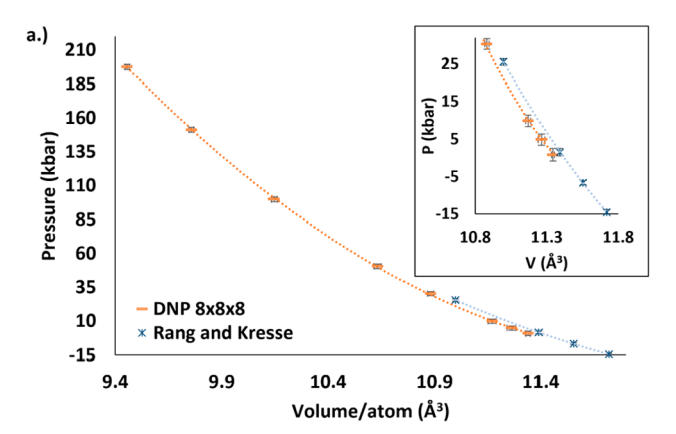
long MD simulations over many different temperatures and hence is challenging with DFT simulations, particularly for large supercell sizes. Good potentials can be expected to show stability throughout the simulation and a steady, logical trend over different temperatures; however, significant deviations can be observed for potentials that fail.

In preparing the DNP to simulate the thermal expansion of MgO rock salt, we created the training configurations starting from the 2 \times 2 \times 2 supercell and running NVT MD simulations at temperatures close to the melting point, around 3000 K. We included configurations from the high-temperature regime as the initial database included only temperatures up to 1000 K. In addition, we adjusted the lattice parameter based on previous DFT studies conducted at high temperatures. We also included distortions in the form of uniform contraction and expansion of the lattice up to 5% to provide additional information. This adaptive-learning process involved six iterations culminating in the addition of 8125 new configurations.

The performance of our DNP can be directly assessed by comparing it to the work by Rang and Kresse⁴⁴ on the same rock salt MgO system using PBE. To make this comparison, we ran MD NPT (constant temperature, constant pressure ensemble) at 2850 K, the same temperature in which they investigated the pressure-volume relationship for solid MgO, for 200 ps for pressure values from 0 to 200 kbar at 0.001 ps per MD step. The temperature and pressure thermostat damping was applied at 0.1 and 1 ps, respectively. We consider the averaged pressures and volumes from the last 50 ps as the equilibrium values at that state (Figure 4a). At the specific point of 0 kbar and 2850 K, Rang and Kresse⁴⁴ found the equilibrium volume per atom to be 11.39 Å³ with a system size of 128 atoms. In comparison, the DNP found the equilibrium volume per atom to be 11.32 Å³ or 0.61% for $4 \times 4 \times 4$ (512) atoms) and 11.34 Å^3 or 0.44% for $8 \times 8 \times 8$ supercells (4096) atoms). This matching trend persists, approaching the highest pressure in which Rang and Kresse did their study at 25 kbar. To test the capability of the potential, we continued investigating up to 200 kbar from which we observed DNP to interpolate untrained states correctly and is stable with maximum volume and pressure errors of 0.04 Å³ and 1.86 kbar, respectively. It is notable that, in contrast to the DFT study, the pressure and volume values from the DNP are direct averages from the MD NPT simulation, while the DFT values were from NVT simulation done at various volumes.

To investigate thermal expansion, we again ran MD NPT simulations at temperatures from 5 to 3000 K. We evaluated the volume and energy of the system as a function of temperature using supercell sizes of 512 and 4096 atoms. We show in Figure S2 that the values from $4\times4\times4$ and $8\times8\times8$ supercells are comparable, which suggests that finite-size effects are minimal. Moreover, no significant deviations in energy or volume are visible, indicating that the training process is successful and the DNP can generate stable long MD simulations at near melting temperatures.

Previous studies have argued that MgO displays non-harmonic behavior. As, 45, 47, 49 Reeber et al. 49 created a quasi-harmonic model by fitting experimental results. Dubrovinsky and Saxena heated the MgO sample and observed nonlinear expansion. Similar findings are also reported by Fiquet et al. Aguado et al. 46 observed a nonharmonic trend by developing a classical interatomic potential with a functional form whose



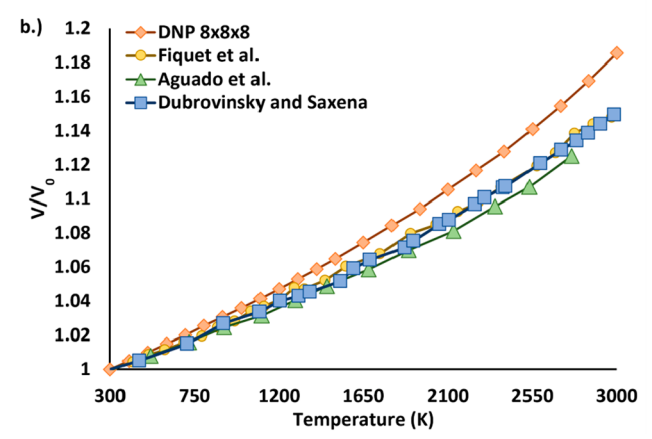


Figure 4. (a) Pressure of solid phase as a function of volume at 2850 K from this study (orange) and Rang and Kresse⁴⁴ (blue); the inset is a close-up at low pressures. (b) Relative expansion of MgO from room temperature as a function of temperature. Orange symbols are from this study, blue symbols are from Dubrovinsky and Saxena,⁴⁵ green symbols are from Aguado, Bernasconi, and Madden,⁴⁶ and yellow symbols are from Fiquet, Richet, and Montagnac.⁴⁷

terms are tailored to encompass the interactions in a MgO system.

We have examined the thermal expansion in MgO. As shown in Figure 4b, the DNP can replicate the nonharmonic trend within less than a 4% difference in relative expansion from experimental results. Likely, these underestimations are due to intrinsic errors from DFT. Unfortunately, such investigations are computationally very challenging using standard DFT for validation. In replicating this trend, we note that the DNP has interpolated correctly for a temperature range of $\sim\!2000$ K, as no information between 1000 and $\sim\!3000$ K was included in the data set. These results are a compelling show of the transferability of the DNP.

We have created versatile machine learning potentials for five different metal oxide systems. We showed a systematic and replicable training protocol for DNPs. The performance validation of these DNPs proved that DNPs could account for multiple oxidation states without explicit information about ionic charges. To facilitate future studies, we demonstrated that DNPs, initially trained on periodic systems and low-temperature regimes, can be augmented with additional configurations to enhance the transferability of the potentials to additional properties. Namely, we show that the MgO DNP can be successfully extended to describe a new MgO polymorph, MgO (100) and (110) surface energies, and thermal expansion. We showed that the MgO DNP could

interpolate a significant pressure and temperature range of \sim 2000 K. With increasing temperature, MgO is shown to display nonharmonic expansion consistent with experimental results. The systematic development of succinct DNPs for the oxides and the demonstration of their success in describing these systems with high fidelity open the possibility of studying ionic systems using DNPs where multiple compositions and/or phases are present.

ASSOCIATED CONTENT

Data Availability Statement

A spreadsheet showing a comparison of energy, volume, and elastic constant of DFT and DNP (XLSX). The compiled potential and training data set can be found on GitHub with DOI 10.5281/zenodo.7278342.

Supporting Information

The Supporting Information is available free of charge at https://pubs.acs.org/doi/10.1021/acs.jpclett.2c03445.

A table listing structure information included in the data set, a figure showing energy as a function of temperature for different supercell sizes, and a figure showing energy as a function of time step at near melting temperatures (PDF)

AUTHOR INFORMATION

Corresponding Author

Wissam A. Saidi — Department of Mechanical Engineering and Materials Science, University of Pittsburgh, Pittsburgh, Pennsylvania 15216, United States; orcid.org/0000-0001-6714-4832; Email: alsaidi@pitt.edu

Authors

Pandu Wisesa – Department of Mechanical Engineering and Materials Science, University of Pittsburgh, Pittsburgh, Pennsylvania 15216, United States

Christopher M. Andolina — Department of Mechanical Engineering and Materials Science, University of Pittsburgh, Pittsburgh, Pennsylvania 15216, United States;
orcid.org/0000-0003-2157-9114

Complete contact information is available at: https://pubs.acs.org/10.1021/acs.jpclett.2c03445

Notes

The authors declare no competing financial interest.

ACKNOWLEDGMENTS

We are grateful to the U.S. National Science Foundation (Award CSSI-2003808). This research was supported in part by the University of Pittsburgh Center for Research Computing through the resources provided. Specifically, this work used the H2P cluster, which is supported by NSF Award OAC-2117681. Also, we acknowledge computational resources from Argonne Leadership Computing Facility, which is a DOE Office of Science User Facility supported under Contract DE-AC02-06CH11357.

REFERENCES

- (1) Pauling, L. Atomic Radii and Interatomic Distances in Metals. J. Am. Chem. Soc. 1947, 69 (3), 542–553.
- (2) van Duin, A. C. T.; Dasgupta, S.; Lorant, F.; Goddard, W. A. ReaxFF: A Reactive Force Field for Hydrocarbons. *J. Phys. Chem. A* **2001**, *105* (41), 9396–9409.

- (3) Yu, J.; Sinnott, S. B.; Phillpot, S. R. Charge optimized many-body potential for the SiO₂ system. *Phys. Rev. B* **2007**, 75 (8), 085311.
- (4) Bartók, A. P.; Payne, M. C.; Kondor, R.; Csányi, G. Gaussian Approximation Potentials: The Accuracy of Quantum Mechanics, without the Electrons. *Phys. Rev. Lett.* **2010**, *104* (13), 136403.
- (5) Shapeev, A. V. Moment Tensor Potentials: A Class of Systematically Improvable Interatomic Potentials. *Multiscale Model. Simul.* **2016**, *14* (3), 1153–1173.
- (6) Wang, H.; Zhang, L.; Han, J.; E, W. DeePMD-kit: A deep learning package for many-body potential energy representation and molecular dynamics. *Comput. Phys. Commun.* **2018**, 228, 178–184.
- (7) Lee, K.; Yoo, D.; Jeong, W.; Han, S. SIMPLE-NN: An efficient package for training and executing neural-network interatomic potentials. *Comput. Phys. Commun.* **2019**, 242, 95–103.
- (8) Sivaraman, G.; Gallington, L.; Krishnamoorthy, A. N.; Stan, M.; Csányi, G.; Vázquez-Mayagoitia, Á.; Benmore, C. J. Experimentally Driven Automated Machine-Learned Interatomic Potential for a Refractory Oxide. *Phys. Rev. Lett.* **2021**, *126* (15), 156002.
- (9) Rosenbrock, C. W.; Gubaev, K.; Shapeev, A. V.; Pártay, L. B.; Bernstein, N.; Csányi, G.; Hart, G. L. W. Machine-learned interatomic potentials for alloys and alloy phase diagrams. *npj comput. mater.* **2021**, *7* (1), 24.
- (10) Kocer, E.; Ko, T. W.; Behler, J. Neural Network Potentials: A Concise Overview of Methods. *Annu. Rev. Phys. Chem.* **2022**, 73 (1), 163–186
- (11) Kulichenko, M.; Smith, J. S.; Nebgen, B.; Li, Y. W.; Fedik, N.; Boldyrev, A. I.; Lubbers, N.; Barros, K.; Tretiak, S. The Rise of Neural Networks for Materials and Chemical Dynamics. *J. Phys. Chem. Lett.* **2021**, *12* (26), 6227–6243.
- (12) Behler, J.; Parrinello, M. Generalized Neural-Network Representation of High-Dimensional Potential-Energy Surfaces. *Phys. Rev. Lett.* **2007**, *98* (14), 146401.
- (13) Schütt, K. T.; Arbabzadah, F.; Chmiela, S.; Müller, K. R.; Tkatchenko, A. Quantum-chemical insights from deep tensor neural networks. *Nat. Commun.* **2017**, *8* (1), 13890.
- (14) Han, J.; Zhang, L.; Car, R.; E, W. Deep Potential: A General Representation of a Many-Body Potential Energy Surface. *Commun. Comput. Phys.* **2018**, DOI: 10.4208/cicp.OA-2017-0213.
- (15) Chu, W.; Saidi, W. A.; Prezhdo, O. V. Long-Lived Hot Electron in a Metallic Particle for Plasmonics and Catalysis: Ab Initio Nonadiabatic Molecular Dynamics with Machine Learning. ACS Nano 2020, 14 (8), 10608–10615.
- (16) Andolina, C. M.; Williamson, P.; Saidi, W. A. Optimization and validation of a deep learning CuZr atomistic potential: Robust applications for crystalline and amorphous phases with near-DFT accuracy. J. Chem. Phys. 2020, 152 (15), 154701.
- (17) Andolina, C. M.; Bon, M.; Passerone, D.; Saidi, W. A. Robust, Multi-Length-Scale, Machine Learning Potential for Ag—Au Bimetallic Alloys from Clusters to Bulk Materials. *J. Phys. Chem. C* **2021**, 125 (31), 17438—17447.
- (18) Andolina, C. M.; Wright, J. G.; Das, N.; Saidi, W. A. Improved Al-Mg alloy surface segregation predictions with a machine learning atomistic potential. *Phys. Rev. Mater.* **2021**, *5* (8), 083804.
- (19) Ryltsev, R. E.; Chtchelkatchev, N. M. Deep machine learning potentials for multicomponent metallic melts: Development, predictability and compositional transferability. *J. Mol. Liq.* **2022**, 349, 118181.
- (20) Zhang, L.; Han, J.; Wang, H.; Saidi, W.; Car, R.; E, W. In Endto-end Symmetry Preserving Inter-atomic Potential Energy Model for Finite and Extended Systems; Curran Associates, Inc.: 2018.
- (21) Saidi, W. A., Shadid, W.; Veser, G. Optimization of High-Entropy Alloy Catalyst for Ammonia Decomposition and Ammonia Synthesis. *J. Phys. Chem. Lett.* **2021**, *12* (21), 5185–5192.
- (22) Gartner, T. E.; Zhang, L.; Piaggi, P. M.; Car, R.; Panagiotopoulos, A. Z.; Debenedetti, P. G. Signatures of a liquid-liquid transition in an ab initio deep neural network model for water. *Proc. Natl. Acad. Sci. U. S. A.* **2020**, *117* (42), 26040–26046.

- (23) Ko, H.-Y.; Zhang, L.; Santra, B.; Wang, H.; E, W.; DiStasio, R. A., Jr.; Car, R. Isotope effects in liquid water via deep potential molecular dynamics. *Mol. Phys.* **2019**, *117* (22), 3269–3281.
- (24) Wang, H.; Yang, W. Force Field for Water Based on Neural Network. J. Phys. Chem. Lett. 2018, 9 (12), 3232–3240.
- (25) Shi, Y.; Doyle, C. C.; Beck, T. L. Condensed Phase Water Molecular Multipole Moments from Deep Neural Network Models Trained on Ab Initio Simulation Data. *J. Phys. Chem. Lett.* **2021**, *12* (42), 10310–10317.
- (26) Niu, H.; Bonati, L.; Piaggi, P. M.; Parrinello, M. Ab initio phase diagram and nucleation of gallium. *Nat. Commun.* **2020**, *11* (1), 2654.
- (27) Wu, J.; Zhang, Y.; Zhang, L.; Liu, S. Deep learning of accurate force field of ferroelectric HfO₂. *Phys. Rev. B* **2021**, *103* (2), 024108.
- (28) Luo, H.; Karki, B. B.; Ghosh, D. B.; Bao, H. Anomalous Behavior of Viscosity and Electrical Conductivity of MgSiO₃ Melt at Mantle Conditions. *Geophys. Res. Lett.* **2021**, 48 (13), e2021GL093573.
- (29) Wang, B.; Chu, W.; Wu, Y.; Casanova, D.; Saidi, W. A.; Prezhdo, O. V. Electron-Volt Fluctuation of Defect Levels in Metal Halide Perovskites on a 100 ps Time Scale. *J. Phys. Chem. Lett.* **2022**, 13 (25), 5946–5952.
- (30) Li, R.; Liu, Z.; Rohskopf, A.; Gordiz, K.; Henry, A.; Lee, E.; Luo, T. A deep neural network interatomic potential for studying thermal conductivity of β -Ga2O3. *Appl. Phys. Lett.* **2020**, *117* (15), 152102.
- (31) Kresse, G.; Furthmüller, J. Efficient iterative schemes for ab initio total-energy calculations using a plane-wave basis set. *Phys. Rev.* B **1996**, *54* (16), 11169–11186.
- (32) Shishkin, M.; Marsman, M.; Kresse, G. Accurate Quasiparticle Spectra from Self-Consistent GW Calculations with Vertex Corrections. *Phys. Rev. Lett.* **2007**, *99* (24), 246403.
- (33) Blöchl, P. E. Projector augmented-wave method. *Phys. Rev. B* **1994**, *50* (24), 17953–17979.
- (34) Thompson, A. P.; Aktulga, H. M.; Berger, R.; Bolintineanu, D. S.; Brown, W. M.; Crozier, P. S.; in 't Veld, P. J.; Kohlmeyer, A.; Moore, S. G.; Nguyen, T. D.; Shan, R.; Stevens, M. J.; Tranchida, J.; Trott, C.; Plimpton, S. J. LAMMPS a flexible simulation tool for particle-based materials modeling at the atomic, meso, and continuum scales. *Comput. Phys. Commun.* **2022**, 271, 108171.
- (35) Jain, A.; Ong, S. P.; Hautier, G.; Chen, W.; Richards, W. D.; Dacek, S.; Cholia, S.; Gunter, D.; Skinner, D.; Ceder, G.; Persson, K. A. Commentary: The Materials Project: A materials genome approach to accelerating materials innovation. *APL Mater.* **2013**, *1* (1), 011002.
- (36) Momma, K.; Izumi, F. VESTA 3 for three-dimensional visualization of crystal, volumetric and morphology data. *J. Appl. Crystallogr.* **2011**, 44 (6), 1272–1276.
- (37) Zhang, L.; Lin, D.-Y.; Wang, H.; Car, R.; E, W. Active learning of uniformly accurate interatomic potentials for materials simulation. *Phys. Rev. Mater.* **2019**, *3* (2), 023804.
- (38) Le Page, Y.; Saxe, P. Symmetry-general least-squares extraction of elastic data for strained materials from ab initio calculations of stress. *Phys. Rev. B* **2002**, *65* (10), 104104.
- (39) Refson, K.; Wogelius, R. A.; Fraser, D. G.; Payne, M. C.; Lee, M. H.; Milman, V. Water chemisorption and reconstruction of the MgO surface. *Phys. Rev. B* **1995**, *52* (15), 10823–10826.
- (40) Tasker, P. W. The stability of ionic crystal surfaces. *Journal of Physics C: Solid State Physics* 1979, 12 (22), 4977–4984.
- (41) Evarestov, R. A.; Bandura, A. V. HF and DFT calculations of MgO surface energy and electrostatic potential using two- and three-periodic models. *Int. J. Quantum Chem.* **2004**, *100* (4), 452–459.
- (42) Jura, G.; Garland, C. W. The Experimental Determination of the Surface Tension of Magnesium Oxide. *J. Am. Chem. Soc.* **1952**, 74 (23), 6033–6034.
- (43) Lazar, P.; Otyepka, M. Accurate surface energies from first principles. *Phys. Rev. B* **2015**, *91* (11), 115402.
- (44) Rang, M.; Kresse, G. First-principles study of the melting temperature of MgO. *Phys. Rev. B* **2019**, 99 (18), 184103.

- (45) Dubrovinsky, L. S.; Saxena, S. K. Thermal Expansion of Periclase (MgO) and Tungsten (W) to Melting Temperatures. *Phys. Chem. Miner.* **1997**, 24 (8), 547–550.
- (46) Aguado, A.; Bernasconi, L.; Madden, P. A. A transferable interatomic potential for MgO from ab initio molecular dynamics. *Chem. Phys. Lett.* **2002**, 356 (5), 437–444.
- (47) Fiquet, G.; Richet, P.; Montagnac, G. High-temperature thermal expansion of lime, periclase, corundum and spinel. *Phys. Chem. Miner.* **1999**, 27 (2), 103–111.
- (48) Alfe, D. Melting Curve of MgO from First-Principles Simulations. *Phys. Rev. Lett.* **2005**, 94 (23), 235701.
- (49) Reeber, R. R.; Goessel, K.; Wang, K. Thermal expansion and molar volume of MgO, periclase, from 5 to 2900 K. *Eur. J. Mineral.* **1995**, 7 (5), 1039–1048.

□ Recommended by ACS

Stability and Equilibrium Structures of Unknown Ternary Metal Oxides Explored by Machine-Learned Potentials

Seungwoo Hwang, Seungwu Han, et al.

AUGUST 11, 2023

JOURNAL OF THE AMERICAN CHEMICAL SOCIETY

READ 🗹

Advancing Accurate and Efficient Surface Behavior Modeling of Al Clusters with Machine Learning Potential

Chongteng Wu, Duanyun Cao, et al.

SEPTEMBER 18, 2023

THE JOURNAL OF PHYSICAL CHEMISTRY C

READ 🗹

High-Accuracy Machine-Learned Interatomic Potentials for the Phase Change Material Ge₃Sb₆Te₅

Wei Yu, Yuzheng Guo, et al.

AUGUST 14, 2023

CHEMISTRY OF MATERIALS

READ 🗹

Predictive Synthesis of Copper Selenides Using a Multidimensional Phase Map Constructed with a Data-Driven Classifier

Emily M. Williamson, Richard L. Brutchey, et al.

AUGUST 04, 2023

JOURNAL OF THE AMERICAN CHEMICAL SOCIETY

READ 🗹

Get More Suggestions >